Supporting Information Part 1 (SI1) for Accessing Distributions of Exchange and Dipolar Couplings in Stiff Molecular Rulers with Cu(II) centres

K. Keller[a], I. Ritsch[a], H. Hintz[b], M. Hülsmann[b], M. Qi[b], F. D. Breitgoff[a], D. Klose[a], Y. Polyhach*[,a], M. Yulikov*[,a], A. Godt*[,b], G. Jeschke[a]

[a]*Laboratory of Physical Chemistry, Department of Chemistry and Applied Biosciences, ETH Zurich, Vladimir-Prelog-Weg 2, 8093 Zurich, Switzerland.*
[b]*Faculty of Chemistry and Center for Molecular Materials (CM_2), Bielefeld University, Universitätsstraße 25, 33615 Bielefeld, Germany*

1. Supplementary Information

1.1. Author contributions

H.H., M.H., M.Q. and A.G. designed the synthetic routes, and H.H., M.H. and M.Q. performed the synthesis of the rulers. I.R. performed and analyzed the UV/Vis experiments, as well as Cu(II)-nitroxide RIDME measurements. F.D.B. acquired the metal–metal DEER measurements. K.K. performed the metal–metal RIDME experiments, lineshape simulations and analysis of the PDS data. I.R. and K.K. recorded the CW EPR data. Y.P. developed the exchange coupling models and contributed to exchange coupling analysis. D.K. and K.K. carried out the DFT calculations. All authors contributed to the design of the research, discussed the results and participated in writing the manuscript.

1.2. Comparison of RIDME and DEER data

The comparison of orientation-averaged DEER and RIDME data is presented in Figure S1 for [Cu-TAHA]–[Cu-TAHA] ruler **3** and [Cu-PyMTA]–[Cu-PyMTA] ruler $\mathbf{1}_5$. Apart from strongly varying background functions

*Corresponding authors: Dr. Yevhen Polyhach (yevhen.polyhach@phys.chem.ethz.ch), Dr. Maxim Yulikov (maxim.yulikov@phys.chem.ethz.ch), Prof. Dr. Adelheid Godt (godt@uni-bielefeld.de)

in the two experiments and some differences in the modulation depth, the data sets from the two methods are consistent for both compounds. As a consequence of background correction, small variations around 0 MHz can be observed in the frequency domain data. The smaller time step $\Delta t = 8$ ns in RIDME experiments versus $\Delta t = 24$ ns in DEER for the [Cu-TAHA]–[Cu-TAHA] ruler **3** leads to extension of the detectable frequency range and thus access to shorter distances or larger exchange couplings for the RIDME-based measurements.

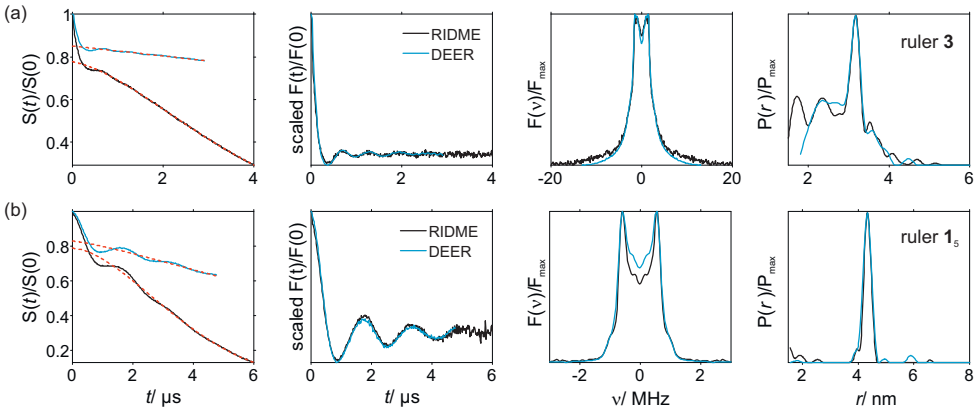

Figure S1: Q-band orientation-averaged RIDME (black) and DEER (blue) measurements at 20 K. (a) [Cu-TAHA]–[Cu-TAHA] ruler **3** and (b) [Cu-PyMTA]–[Cu-PyMTA] ruler $\mathbf{1}_5$. From left to right: Primary data $S(t)$ and corresponding background fit (red, dashed lines); modulation depth-scaled form factors in time domain $F(t)$; form factors in frequency domain $F(\nu)$; resulting distance distribution $P(r)$.

For the [Cu-PyMTA]–[Cu-PyMTA] ruler $\mathbf{1}_3$ some larger variations were observed in different measurement sessions as shown in Figure S2. These variations might be related to residual orientation selection, a difference in noise level and deviations of the background decay shape from the background models.

Nevertheless, the resulting apparent distance distributions agree qualitatively and vary mainly in the relative weighting of the bimodal distribution. Consequently, resulting exchange coupling distributions using the same input distance distribution exhibit the same features, with different weightings in the exchange coupling distributions as shown in Figure S3. The behaviour of the exchange coupling distribution is studied for different input distance distributions in Section 1.7.

Note that different mixing times were applied in different measurement

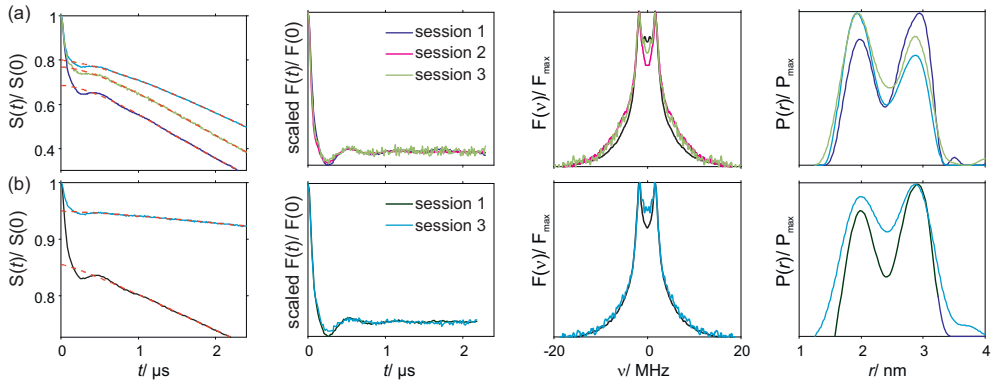

Figure S2: Q-band orientation-averaged RIDME (a) and DEER (b) measurements for [Cu-TAHA]–[Cu-TAHA] ruler $\mathbf{1}_3$ at 20 K. Different measurement sessions (see text) are color coded. From left to right: Primary data $S(t)$ and corresponding background fit (red, dashed lines); modulation depth-scaled form factors in time domain $F(t)$; form factors in frequency domain $F(\nu)$; resulting distance distribution $P(r)$.

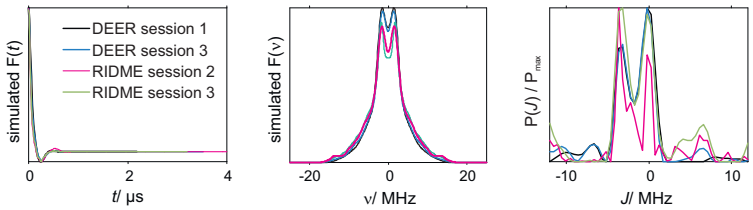

Figure S3: Extracted exchange-coupling distributions for the [Cu-TAHA]–[Cu-TAHA] ruler $\mathbf{1}_3$ at 20 K. A Gaussian distance distribution of $r_{\mathrm{mean}} = 3.0$ nm, $\sigma_r = 0.2$ was used for all data sets. Color coding maintained from Figure S2. From left to right: Time-domain form factor fit F(t); frequency-domain form factor fit F(v); resulting exchange coupling distribution P(J).

sessions of the [Cu-TAHA]–[Cu-TAHA] ruler $\mathbf{1}_3$: $T_{\mathrm{mix}} = 160$ μs in session 1, $T_{\mathrm{mix}} = 40$ μs in session 2 and $T_{\mathrm{mix}} = 80$ μs in session 3. In session 3 the influence of mixing time on the form factor shape was studied for data detected at the maximum of the copper spectrum. No strong deviations were observed in RIDME form factors with changing mixing time for the different Cu-rulers as shown in Figure S4.

Figure S5 shows the RIDME data for the shortest [Cu-PyMTA]–[Cu-PyMTA] ruler $\mathbf{1}_1$. The modulation depth is strongly reduced in this sample compared to the [Cu-PyMTA]–[Cu-PyMTA] rulers $\mathbf{1}_3$ and $\mathbf{1}_5$ with larger interspin distances indicating the presence of strong couplings that are not excited by the RIDME experiment.

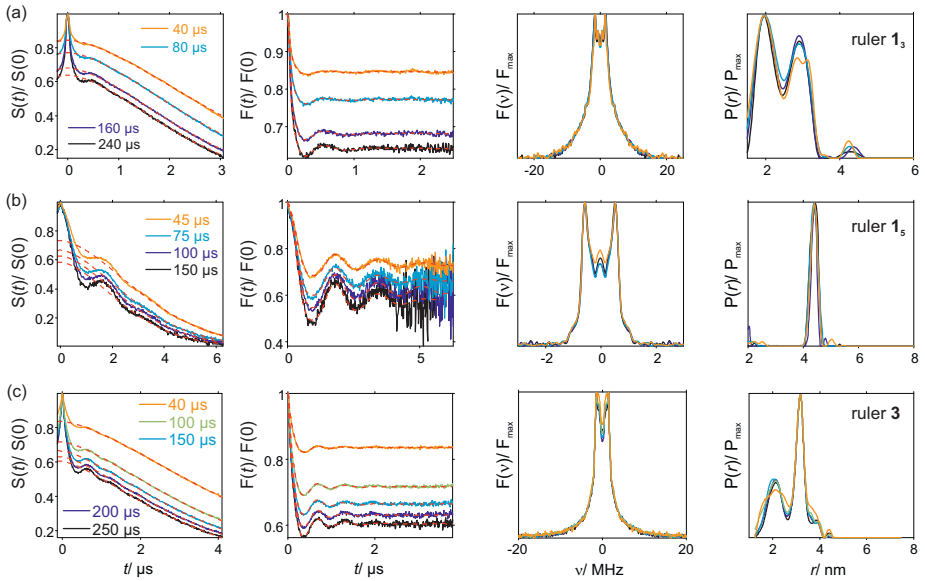

Figure S4: Q-band RIDME data for the different Cu(II)-Cu(II) rulers at 20 K. (a) [Cu-PyMTA]–[Cu-PyMTA] ruler $\mathbf{1}_3$, (b) [Cu-PyMTA]–[Cu-PyMTA] ruler $\mathbf{1}_5$, (c) [Cu-TAHA]–[Cu-TAHA] ruler **3**. Columns of subfigures from left to right: (first column) Primary data $S(t)$, with color coding for different mixing times shown directly in the subfigures, and corresponding background fits (dashed red lines); (second column) form factor traces in time domain $F(t)$ along with their fits (color coding for the form factor data as in the first column, form factor fits are shown as dashed red lines); (third column) form factors in frequency domain $F(\nu)$ (same color coding as in the first two columns); apparent distance distributions $P(r)$ computed, assuming a dipolar kernel without any exchange contributions (the standard DeerAnalysis kernel).

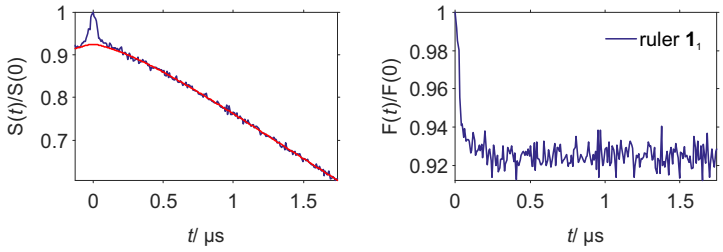

Figure S5: Q-band RIDME data for [Cu-PyMTA]–[Cu-PyMTA] ruler $\mathbf{1}_1$ at 20 K, $T_{\mathrm{mix}} = 150\ \mu$s. Left: Primary data $S(t)$ and corresponding background fit (dashed red lines). Right: Form factor traces in time domain $F(t)$.

*1.3. PDS data for the [Cu-TAHA]–[Cu-TAHA] ruler **3** at different field positions*

Figure S6 shows RIDME (a-d) and DEER (e-h) data detected at different field positions as well as the field average (black lines). We find it con-

venient to analyse the apparent distance distributions in order to separate artefact contributions from the contribution due to the exchange couplings. Clear differences can be observed for different detection positions in particular in the yellow-shaded area in Figure S6 (d, h). This is expected from the anisotropy of the Cu-TAHA spectrum. The peak in the green-shaded area is always present and corresponds to the anticipated Cu-Cu distance of [Cu-TAHA]–[Cu-TAHA] ruler **3**. Additional small peaks can be observed in the red-shaded area, that do not vary strongly between different detection positions (small changes are related to different regularization parameters due to variations in the noise level). We further notice one or several peaks in the purple-shaded area, which extend in the yellow-shaded area. The large variations in the purple- and yellow-shaded areas must be mainly attributed to orientation selection effects and differences in the signal-to-noise ratio for different detection fields, while peaks of small amplitude, or with strong overlap with neighboring peaks most likely result from limitations of Tikhonov regularization for the complex shape of the apparent distance distribution. In the presence of a narrow peak of significant amplitude, a broad 'background' distance distribution breaks into a collection of partially overlapping peaks of approximately the same width as the main narrow peak. Note also that these variations are of the order of inaccuracy of the computed apparent distance distributions based on PDS data from different measurement sessions. This remaining broad peak cannot be explained by orientation-selection effects and is attributed to distributed exchange couplings.

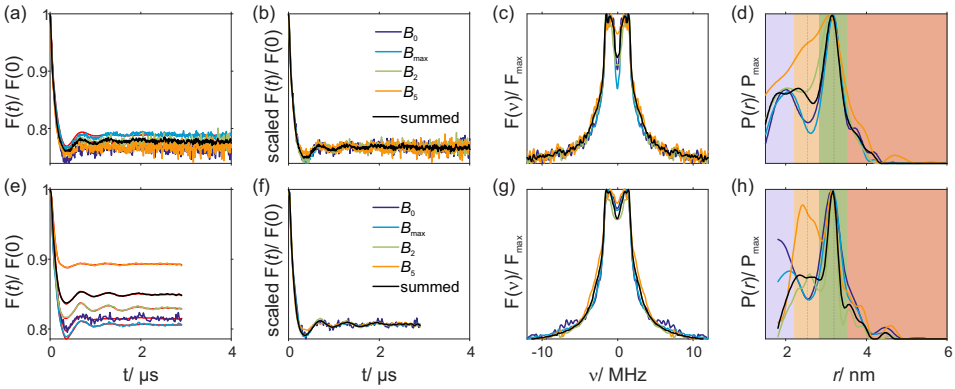

Figure S6: Q-band RIDME (a-d) and DEER (e-h) data for [Cu-TAHA]–[Cu-TAHA] ruler **3** at 20 K, detected at different field positions within the Cu(II) spectrum. Maximum field $B_{\max}$, $B_0 = B_{\max} + 150$ G (DEER)/ $B_{\max} + 80$ G (RIDME, the smaller offset was chosen for better data quality), $B_2 = B_{\max} - 300$ G, , $B_5 = B_{\max} - 750$ G. (a, e) Background-corrected form factors and corresponding fits (red lines), (b, f) scaled form factors, (c, g) frequency domain form factors and (d, h) apparent distance distributions, computed using the non-perturbed dipolar kernel without exchange contributions.

1.4. RIDME background decay

Figure S7 shows RIDME measurements performed on Cu-PyMTA and Cu-TAHA. Importantly, those data sets do not show significant contributions from residual hyperfine couplings to surrounding nuclei with long-lasting oscillations. For Cu-TAHA, a sharp artefact peak at zero time and at $d_2 - d_1$ is observed, which most likely stems from echo-crossings.[1,2] Such an artefact may generate low-intensity apparent distance peaks at $r < 2$ nm. While this artefact can be in principle filtered out at the data processing stage,[1] here we did not do this, assuming its amplitude to be small enough to allow for sufficiently good data analysis quality without such filtering.

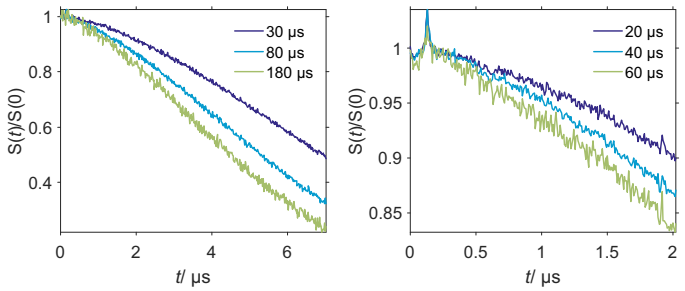

Figure S7: Q-band RIDME background decay at 20 K and different mixing times (color coded). (a) Cu-PyMTA and (b) Cu-TAHA.

1.5. Model of the coupled exchange and distance distributions

Within this model, distance and exchange coupling distributions are assumed to have a simple regular form. For both types of couplings we considered monomodal Gaussian and Lorentzian distributions. Thus, the model is parameterized by four adjustable parameters, namely the mean and the widths of both the distance and the exchange coupling distribution. Recall that within the model both distributions are considered to be coupled, i.e. every exchange coupling value from $J(r)$ corresponds to a particular distance value in $P(r)$, see Figure S8. Finding the best match between simulated and experimental frequency domain data for the [Cu-PyMTA]–[Cu-PyMTA] compounds $\mathbf{1}_3$ and $\mathbf{1}_5$ was realized by a multistep grid search in the four-parameter space.

Compound $\mathbf{1}_5$. The initial search for both the Gaussian and the Lorentzian distribution was performed on a large rough grid comprising the following parameter ranges: r_{mean} from 4.3 to 5.0 nm, step = 0.1 nm; σ_r from 0.025 to 0.225 nm, step = 0.050 nm; J_{mean} from -8.0 to 8.0 MHz, step 0.1 MHz and σ_J from 0.025 to 0.225, step 0.050 MHz. For both Gaussian and Lorentzian distributions, a global minimum characterized by the absence of the exchange coupling was located on this step, see Figure S9. Associated distance distributions in terms of mean and width were similar in the two cases.

Around the global minimum on the rough grid, consecutive searches were conducted using finer grids (with final increments of 0.025 for each parameter varied). The 10 best solutions of the finest grid together with the spectrum corresponding to the best rmsd model are given in Figure S10 .

Compound $\mathbf{1}_3$. The grid search procedure was conducted similar to the previous case of the compound $\mathbf{1}_5$. Initially, the following rough large grid was used for both Gaussian and Lorentzian distributions: r_{mean} from 2.4 to

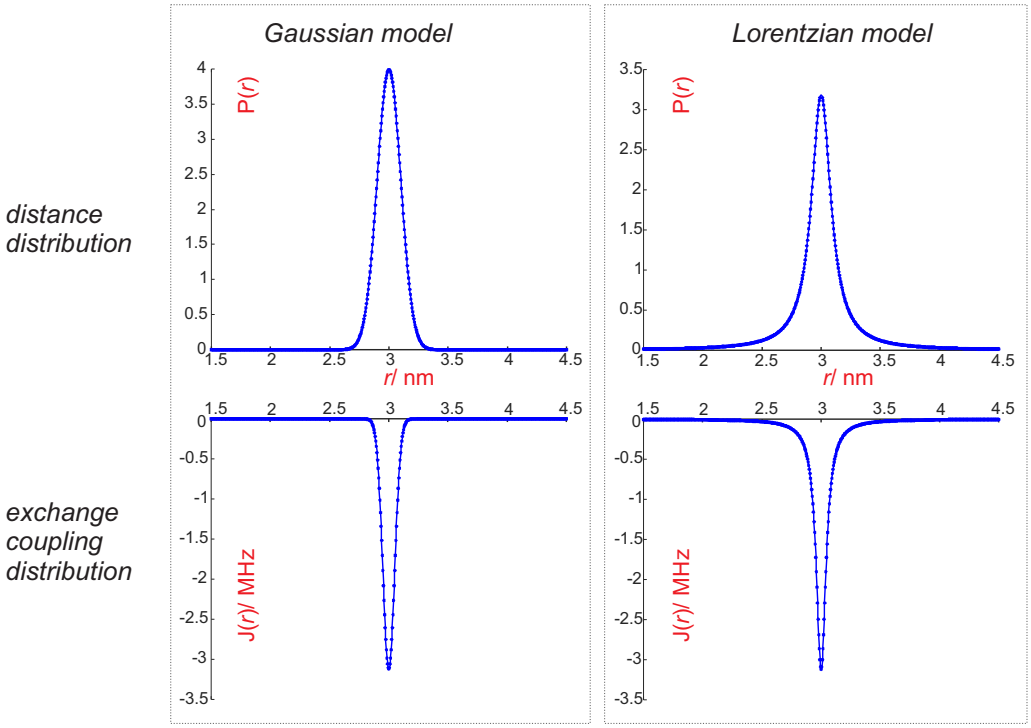

Figure S8: Illustration of the model of coupled Gaussian/Lorentzian distance and exchange couplings distributions.

3.4 nm, step = 0.1 nm; σ_r from 0.05 to 0.4 nm, step = 0.05 nm; J_{mean} from -12.0 to 2.0 MHz, step 1 MHz and σ_J from 0.01 to 0.26, step 0.025 MHz. The best 20 models are given in Figure S11.

In case of the Lorentzian distribution, a clear global minimum was located on this step, whereas for the Gaussian distribution, two solutions of similar quality were identified. Hence, subsequent finer grid searches were conducted around both minima. The results of the fine grid search for [Cu-PyMTA]–[Cu-PyMTA] compound $\mathbf{1}_3$ are given in Figure S12 – with a final increment of 0.01 for each parameter.

(a)

r_{mean}/nm	σ_r/nm	J_{mean}/MHz	σ_J/MHz	RMSD
4.5000	0.0750	0	0.2250	0.0180
4.5000	0.0750	0	0.0250	0.0181
4.5000	0.0750	0	0.0750	0.0181
4.5000	0.0750	0	0.1250	0.0182
4.5000	0.0750	0	0.1750	0.0183
4.5000	0.1250	0	0.1750	0.0186
4.5000	0.1250	0	0.0250	0.0188
4.5000	0.1250	0	0.1250	0.0189
4.5000	0.1250	0	0.2250	0.0190
4.5000	0.1250	0	0.0750	0.0192
4.3000	0.0750	-0.1000	0.2250	0.0235
4.3000	0.0750	-0.1000	0.1750	0.0236
4.5000	0.1750	0	0.1250	0.0240
4.5000	0.1750	0	0.2250	0.0241
4.4000	0.0750	-0.1000	0.0250	0.0242
4.3000	0.0750	-0.1000	0.1250	0.0244
4.5000	0.1750	0	0.0250	0.0245
4.5000	0.1750	0	0.0750	0.0246
4.5000	0.1750	0	0.1750	0.0247
4.6000	0.1250	0.1000	0.0250	0.0251

(b)

r_{mean}/nm	σ_r/nm	J_{mean}/MHz	σ_J/MHz	RMSD
4.5000	0.1750	0	0.1250	0.0180
4.5000	0.1750	0	0.2250	0.0181
4.5000	0.1750	0	0.0250	0.0181
4.5000	0.1750	0	0.0750	0.0181
4.5000	0.1750	0	0.1750	0.0182
4.5000	0.2250	0	0.1750	0.0198
4.5000	0.2250	0	0.0250	0.0199
4.5000	0.2250	0	0.2250	0.0199
4.5000	0.2250	0	0.1250	0.0202
4.5000	0.2250	0	0.0750	0.0202
4.4000	0.1250	-0.1000	0.0250	0.0210
4.5000	0.1250	0	0.0250	0.0211
4.5000	0.1250	0	0.0750	0.0211
4.5000	0.1250	0	0.1250	0.0211
4.5000	0.1250	0	0.2250	0.0215
4.5000	0.1250	0	0.1750	0.0215
4.4000	0.1750	-0.1000	0.0750	0.0223
4.4000	0.1750	-0.1000	0.0250	0.0227
4.3000	0.1750	-0.1000	0.2250	0.0227
4.3000	0.1250	-0.1000	0.2250	0.0228

Figure S9: Best 20 solutions of the initial search using a rough large grid for the [Cu-PyMTA]–[Cu-PyMTA] compound $\mathbf{1}_5$: (a) For Lorentzian distribution shapes, (b) for Gaussian distribution shapes. Relative noise level in the fitting target (experimental frequency spectrum, see Figure 6(a) and Figure S10) is 0.0014.

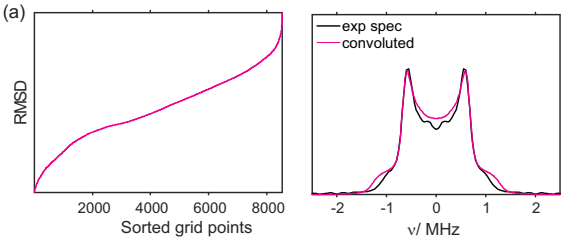

r_{mean}/nm	σ_r/nm	J_{mean}/MHz	σ_J/MHz	RMSD
4.5000	0.1000	0	0.0600	0.0171
4.5000	0.1000	0	0.0350	0.0172
4.4500	0.1000	-0.0250	0.0850	0.0173
4.5000	0.1000	0	0.0850	0.0173
4.5000	0.1000	0	0.0100	0.0174
4.4500	0.1000	-0.0250	0.0350	0.0177
4.4750	0.1000	-0.0250	0.0350	0.0177
4.4750	0.1000	0	0.0600	0.0178
4.4750	0.1000	-0.0250	0.0100	0.0178
4.4500	0.1000	-0.0250	0.0600	0.0179
4.5750	0.1750	-0.0250	0.0850	0.0179
4.5750	0.1750	-0.0250	0.0600	0.0179
4.6000	0.1750	-0.0250	0.0350	0.0179
4.6000	0.1750	-0.0250	0.0100	0.0180
4.5750	0.2000	-0.0250	0.0600	0.0182
4.6000	0.2000	0	0.0100	0.0182
4.6250	0.1750	0	0.0350	0.0182
4.5750	0.2000	-0.0250	0.0850	0.0183
4.6000	0.1750	0	0.0850	0.0183
4.6000	0.2000	0	0.0850	0.0183

Figure S10: Results of the grid search procedure for [Cu-PyMTA]–[Cu-PyMTA] compound $\mathbf{1}_5$ using the final finest parameter grid. (a) For Lorentzian distribution shapes; (b) for Gaussian distribution shapes. From left to right: sorted rmsd plot for all grid models; experimental spectrum (black) superimposed by the best-fit solution (pink line – for Lorentzian and blue line – for Gaussian distributions); Parameters of the 10 best grid models. Relative noise level of the experimental spectrum is 0.0014.

(a)

r_{mean}/nm	σ_r/nm	J_{mean}/MHz	σ_J/MHz	RMSD
2.5000	0.1500	-5.0000	0.0600	0.0038
2.7000	0.1000	-5.0000	0.0600	0.0039
2.4000	0.2000	-6.0000	0.0600	0.0040
2.4000	0.2500	-6.0000	0.0600	0.0042
2.6000	0.1000	-5.0000	0.2100	0.0042
2.5000	0.1500	-6.0000	0.0600	0.0043
2.4000	0.1500	-5.0000	0.0600	0.0043
2.6000	0.1000	-5.0000	0.0850	0.0043
2.5000	0.1000	-5.0000	0.0600	0.0044
2.5000	0.2000	-6.0000	0.0600	0.0044
2.5000	0.2000	-5.0000	0.0600	0.0044
2.6000	0.1000	-5.0000	0.2350	0.0044
2.4000	0.1500	-6.0000	0.0850	0.0044
2.4000	0.2000	-5.0000	0.0600	0.0045
2.6000	0.1000	-5.0000	0.1850	0.0045
2.5000	0.2000	-5.0000	0.0350	0.0045
2.9000	0.1000	-4.0000	0.2350	0.0046
2.4000	0.1500	-6.0000	0.0600	0.0046
2.4000	0.1000	-2.0000	0.0600	0.0046
2.4000	0.1000	-2.0000	0.0350	0.0046

(b)

r_{mean}/nm	σ_r/nm	J_{mean}/MHz	σ_J/MHz	RMSD
2.5000	0.3500	-5.5000	0.0850	0.0028
2.5000	0.3000	-5.5000	0.0850	0.0029
2.5000	0.3500	-5.2500	0.0850	0.0030
2.5000	0.2000	-5.5000	0.0850	0.0031
2.5000	0.2500	-5.5000	0.0850	0.0031
2.5000	0.3000	-5.2500	0.0850	0.0031
2.6000	0.3500	-6.7500	0.0600	0.0032
2.5000	0.3500	-5.7500	0.0850	0.0032
2.7000	0.3500	-8.7500	0.0850	0.0033
2.5000	0.2500	-5.2500	0.0850	0.0033
2.7000	0.3500	-8.5000	0.0850	0.0033
2.5000	0.1500	-5.5000	0.0850	0.0034
2.7000	0.3500	-8.2500	0.0850	0.0034
2.7000	0.3500	-9.0000	0.0850	0.0034
2.6000	0.3500	-7.0000	0.0600	0.0034
2.6000	0.3500	-6.5000	0.0600	0.0035
2.7000	0.3000	-8.2500	0.0850	0.0035
2.5000	0.3000	-5.7500	0.0850	0.0035
2.7000	0.3500	-8.0000	0.0850	0.0035
2.5000	0.2000	-5.2500	0.0850	0.0035

Figure S11: Best 20 solutions of the initial search using a rough large grid for [Cu-PyMTA]–[Cu-PyMTA] compound $\mathbf{1}_3$: (a) For Lorentzian distribution shapes, (b) for Gaussian distribution shapes. The relative noise level of the fitting target (experimental frequency spectrum, Figure 6(b) and Figure S12) is 0.00031.

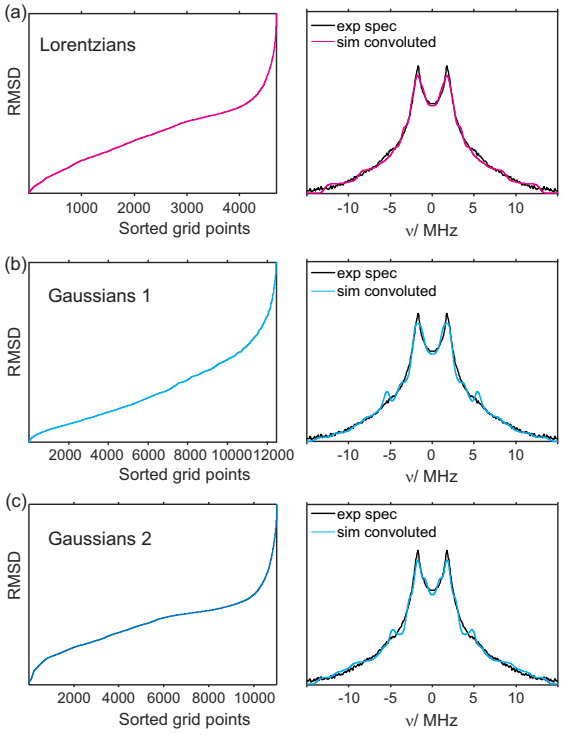

r_{mean}/nm	σ_r/nm	J_{mean}/MHz	σ_J/MHz	RMSD
2.5300	0.0900	-5.3800	0.0400	0.0021
2.5300	0.0800	-5.3700	0.0400	0.0022
2.5300	0.0900	-5.4000	0.0400	0.0022
2.5300	0.0800	-5.3900	0.0400	0.0022
2.5300	0.0900	-5.4100	0.0400	0.0022
2.5200	0.0900	-5.3300	0.0600	0.0022
2.5300	0.0900	-5.3700	0.0400	0.0022
2.5300	0.0900	-5.3900	0.0400	0.0022
2.5300	0.0900	-5.3600	0.0400	0.0022
2.5300	0.0800	-5.4000	0.0400	0.0022
2.7900	0.3600	-8.1900	0.1000	0.0024
2.7900	0.3500	-8.1700	0.1000	0.0024
2.7900	0.3600	-8.1500	0.1000	0.0024
2.7900	0.3600	-8.1400	0.1000	0.0024
2.7900	0.3600	-8.1200	0.1000	0.0024
2.7900	0.3600	-8.2000	0.1000	0.0024
2.7900	0.3500	-8.1800	0.1000	0.0024
2.7900	0.3600	-8.1700	0.1000	0.0024
2.7900	0.3500	-8.1900	0.1000	0.0024
2.7900	0.3600	-8.1300	0.1000	0.0024
2.5000	0.1600	-5.5500	0.0800	0.0025
2.5000	0.1600	-5.5400	0.0800	0.0025
2.5000	0.1800	-5.5500	0.0800	0.0025
2.5000	0.1700	-5.5400	0.0800	0.0025
2.5000	0.1600	-5.5600	0.0800	0.0025
2.5000	0.1700	-5.5600	0.0800	0.0025
2.5000	0.1700	-5.5500	0.0800	0.0025
2.5000	0.1700	-5.5300	0.0800	0.0025
2.5000	0.1700	-5.5200	0.0800	0.0026
2.5000	0.1700	-5.5100	0.0800	0.0026

Figure S12: Summary of the grid search procedure for [Cu-PyMTA]–[Cu-PyMTA] compound $\mathbf{1}_3$ using the final (finest) parameter grid. (a) Lorentzian distributions; (b) Gaussian distributions, solution 1. (c) Gaussian distributions, solution 2. From left to right: sorted rmsd plot for all grid models; experimental spectrum (black) superimposed by the best-fit solution (pink line − for Lorentzian and blue lines − for Gaussian distributions); obtained parameters for the 10 best grid models. S/N of the experimental spectrum is 0.00031.

1.6. Validation of regularization in the exchange-coupling domain

This approach is based on a procedure of solving a system of linear equations by a kernel inversion with subsequent regularization in the exchange coupling domain. It is akin to the approach used to extract distance distributions $P(r)$ from time domain PDS data with a $K(t, r)$ kernel. In order to extract exchange coupling distribution, a new $K(t, J)$ kernel is used. It is composed of a set of time-domain traces each representing fully-orientational averaged data for a single J-coupling value and the same distance distribution, which must be known or estimated beforehand. Exchange-coupling values are equidistant within a certain range, while in the time-domain dimension, the number of points and the time increments are a matter of choice. Hence, depending on the dimensionality of the J-coupling and the time-domain dimensions, the resulting $K(t, J)$ kernel can be a square matrix – when both dimensions are equal – or a rectangular matrix. In case of a square matrix with non-zero determinant, the solution could, in principle, be computed via matrix inversion (matrix pseudo-inversion for a rectangular or singular square matrix). The stability of such a solution can be described by a condition number of the matrix, for instance, the ratio between the largest and smallest singular value. The higher the condition number is, the more ill-conditioned is the problem and the more unstable towards noise is the solution obtained by simple kernel inversion. If the determinant is zero, the condition number is infinity, and the matrix is not even invertible. Note that for calculating distance distributions $P(r)$ condition numbers have been used together with Tikhonov regularization for tackling the problem of ill-posedness.[3] In case of a non-square matrix, the condition number refers to a solution of the set of linear equations in a least-square sense, as it can be obtained by singular value decomposition. For, both, square and non-square matrices, large condition numbers require strong regularization that artificially broadens the parameter distributions.

Before applying a regularization approach to extract exchange-coupling distributions from PDS data of the compounds studied here, we validated the approach using simulated data sets representing the following regimes: monomodal distribution of exchange coupling around zero; monomodal distribution of exchange coupling around some non-zero value; more complex (bimodal) and broad exchange coupling distribution as well as the influence of the width of the underlying distance distribution on the stability of extracting $P(J)$.

The performance of the square $K(t, J)$ kernel with a moderately broad

distance distribution (σ_r=0.08 nm) for extracting exchange coupling distributions with zero and non-zero mean values is summarized in Figures S13 and S14, respectively.

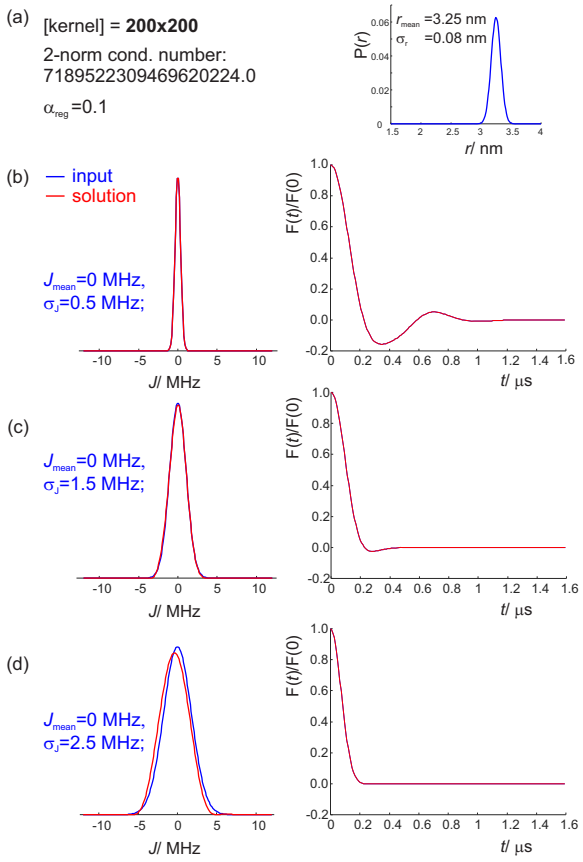

Figure S13: Extracting exchange coupling distributions by $K(t, J)$ kernel inversion and regularization in the exchange coupling domain. Input exchange coupling distribution is centered at zero, distribution width is varied. Kernel dimensionality and underlying distance distribution is kept unchanged for all $P(J)$ width values. (a) Parameters of the $K(t, J)$ kernel and the underlying distance distribution; (b, c, d) input (blue) and output (red) exchange coupling distributions (*left*) and corresponding time domain data (*right*).

Using a square 200×200 $K(t, J)$ kernel with a very large 2-norm condition number, Gaussian $P(J)$ distributions with widths up to 1.5 MHz were extracted perfectly from the time domain data, Figure S13(b, c). The performance of the exchange-coupling extraction deteriorated only slightly upon further increasing of the distribution width up to 2.5 MHz, Figure S13(d).

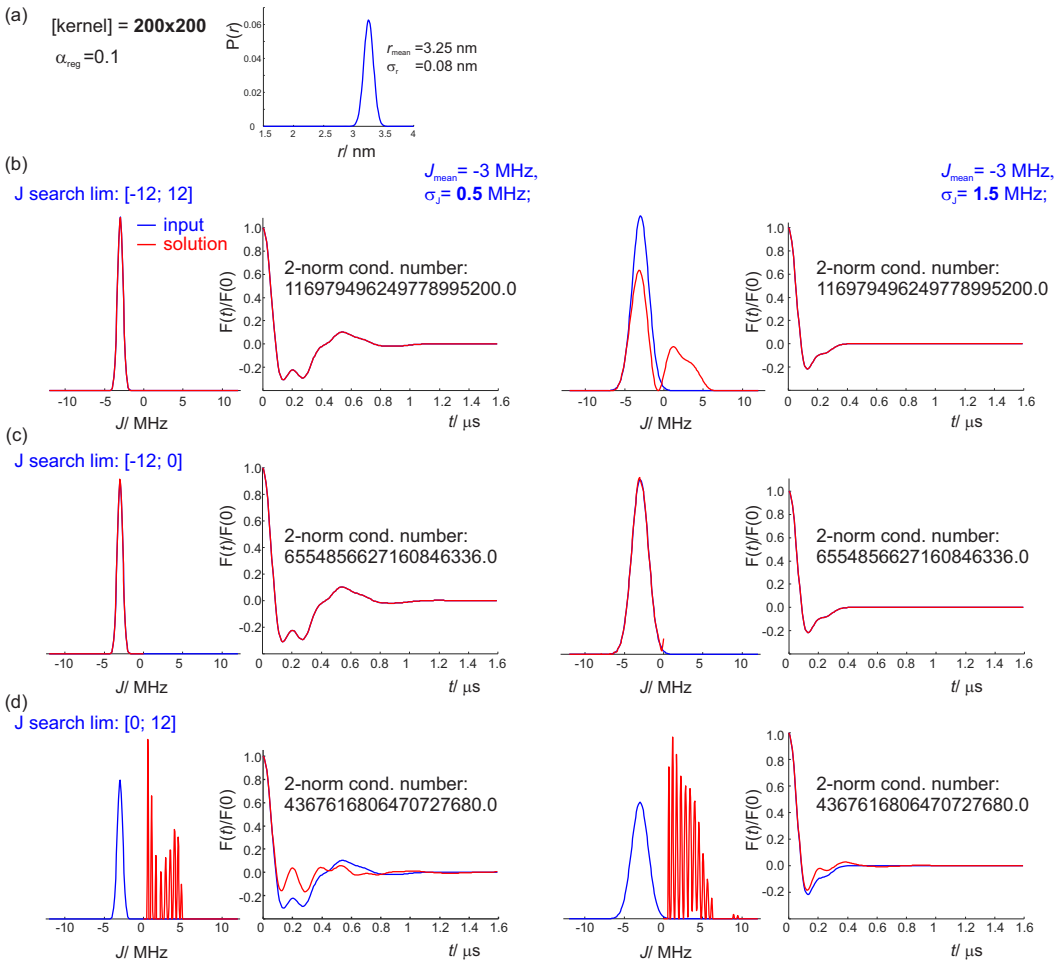

Figure S14: Extracting exchange-coupling distributions by $K(t, J)$ kernel inversion and regularization in the exchange coupling domain. The input exchange-coupling distribution is centered at -3 MHz in all cases, values of σ_J tested are 0.5 MHz (*left panel*) and 1.5 MHz (*right panel*). Kernel dimensionality and underlying distance distribution is kept constant in all cases. (a) Parameters of the $K(t, J)$ kernel and the underlying distance distribution; (b, c, d) input (blue) and output (red) exchange coupling distributions (*left*) and corresponding time domain data (*right*). Limits for the J-coupling values used for the back-calculation of the exchange coupling in each of the cases (b, c) and (d) are indicated in *blue*.

Shifting the mean of the $P(J)$ distribution away from zero caused an immediate negative effect on the precision of the exchange-coupling computation. While a narrow $P(J)$ distribution with $\sigma_J = 0.5$ MHz was recovered

perfectly (Figure S14(b), left), calculation of a broader exchange coupling distribution with $\sigma_J = 1.5$ MHz failed despite of a perfect apparent match observed in the time domain (Figure S14(b), right). The precision of the procedure was restored for both exchange coupling distribution widths by confining the search to the ferromagnetic regime only (where the actual solution is), see Figure S14(c). When enforcing a search within the antiferromagnetic range only, back-calculation of the exchange-coupling distributions fails as expected, see Figure S14(d). However, the fit in time domain does not completely fail, but exhibits most of the correct frequency contributions with some intensity deviations. These are relatively large in the case of the narrow exchange coupling distribution ($\sigma_J = 0.5$ MHz), but relatively small in the case of the broader distribution ($\sigma_J = 1.5$ MHz). Consequently, differentiation of anti- and ferromagnetic coupling may be ambiguous.

We conclude that using square $K(t, J)$ kernels with large condition numbers is only applicable for rather narrow exchange coupling distributions. Errors in the exchange coupling extraction procedure upon increasing the width of the $P(J)$ distribution may be difficult to recognize.

The precision of extracting exchange couplings by regularization in the J-coupling domain for broad and complex exchange coupling distributions could be strongly improved by using non-square $K(t, J)$ kernels of the type $[n, m]$ with $m > n$ (i.e. more points in the time-domain dimension). This is illustrated in Figures S15 and S16 for the situation of a very narrow (σ_{r}=0.04 nm) and a broader (σ_{r}=0.08 nm) underlying distance distributions, respectively.

For the very narrow distance distribution, extracting $P(J)$ fails when the square 200×200 $K(t, J)$ kernel with a large condition number of $3.3119 \cdot 10^{18}$ is used, Figure S15(b). Increasing the number of points in time domain to 1100, thus reaching the kernel dimensionality $[200 \times 1100]$ and a condition number of 1072, restores the accuracy of the exchange coupling calculation, Figure S15(c). Note that a further increase in the number of points in time domain had virtually no effect on the quality of the exchange coupling calculation and the condition number did not decrease either, Figure S15(d).

In the case of the broader underlying distance distribution with $\sigma_r = 0.08$, increasing the number of points in the time-domain dimension did not lead to recovery of the correct exchange coupling distribution. Furthermore, at the kernel dimension of 200×1100 the condition number was still as large as $5.5453 \cdot 10^7$ and it did not further reduce significantly upon increasing the number of time-domain points (Figure S16(b, c) *left*). However, accu-

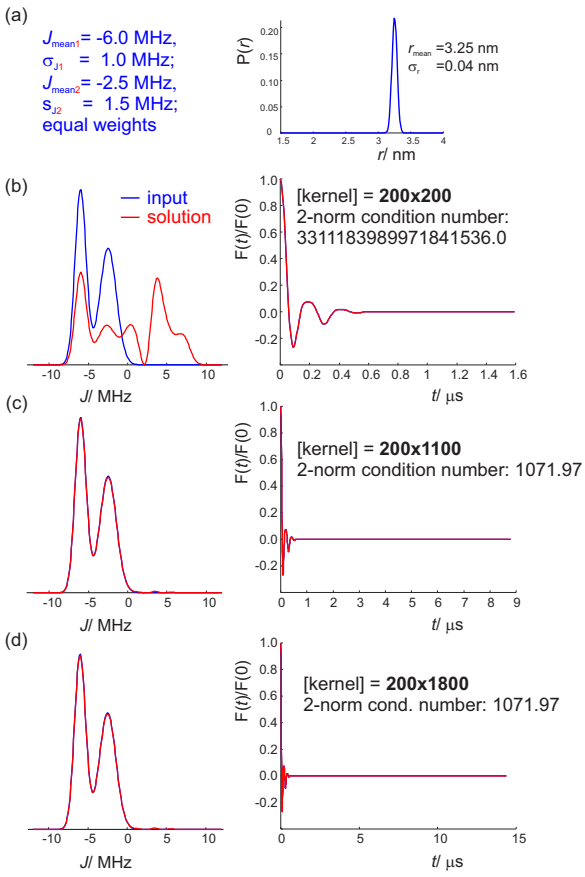

Figure S15: Extracting the exchange coupling distribution by $K(t, J)$ kernel inversion and regularization in the exchange coupling domain. The input exchange coupling distribution is broad and bimodal. The underlying distance distribution (with r_{mean}=3.25 nm and σ_{r}=0.04 nm) is kept constant in all cases, while the kernel dimensionality is varied. (a) Parameters of the input exchange coupling distributions and the underlying distance distribution; (b, c, d) input (blue) and output (red) exchange coupling distributions (*left*) and corresponding time-domain data (*right*).

rate reconstruction of the exchange coupling distribution could be achieved by decreasing the resolution in the exchange-coupling domain, which was accompanied with a decrease of the condition number of the (non-square) $K(t, J)$ kernel used (Figure S16(b, c) *right*). Such an approach is important from a practical point of view, as the resolution of the exchange-coupling dimension can always be reduced while running the algorithm. However, increasing the number of points in time domain may not be possible (e.g.

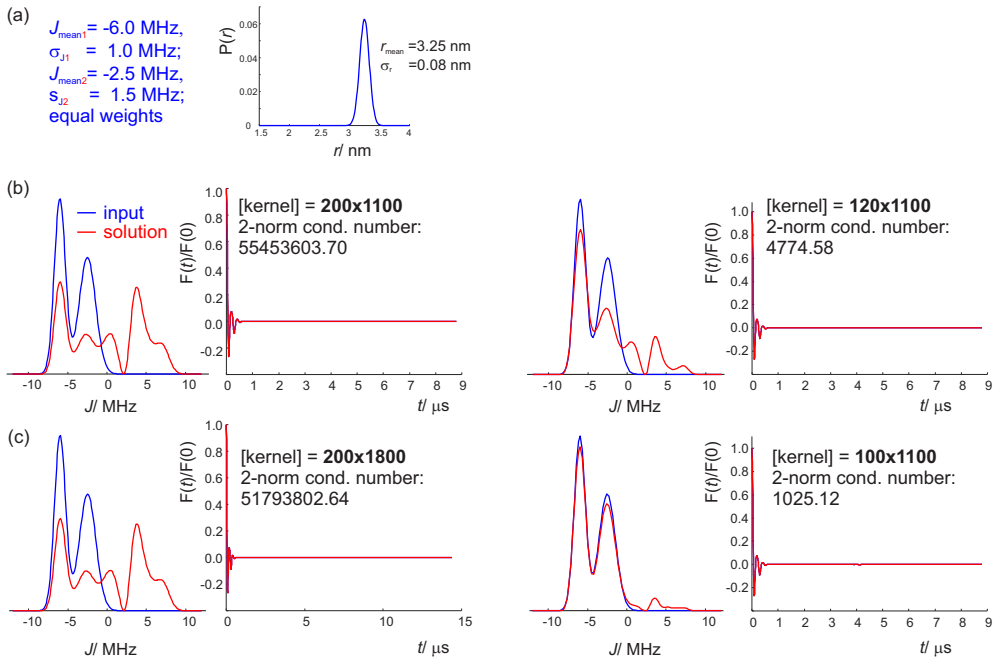

Figure S16: Extracting the exchange coupling distribution by $K(t, J)$ kernel inversion and regularization in the exchange coupling domain. The input exchange coupling distribution is broad and bimodal. The underlying distance distribution (with r_{mean}=3.25 nm and σ_r=0.08 nm) is kept constant in all cases, while the kernel dimensionality is varied. (a) Parameters of the input exchange coupling distribution and the underlying distance distribution; (b, c, d) input (blue) and output (red) exchange coupling distributions (*left*) and corresponding time domain data (*right*).

due to relaxation). Of course, one should keep in mind that reducing the number of points in the exchange-coupling dimension reduces resolution of the exchange-coupling distribution. From the two examples in Figures S15 and S16 it is also clear that it is important to have a narrow underlying distance distribution. We may conclude that extracting distributions of exchange couplings by regularization is currently limited to cases where the distance distribution is narrow and can be independently estimated.

We further conclude that long time-domain data traces together with only moderate resolution in the exchange-coupling domain work best, leading to non-square kernels. Table 1 gives the kernel dimensions used in the analysis of the experimental data and resulting 2-norm condition numbers. The exchange coupling range was from -12 to 12 MHz (compounds $\mathbf{1}_3$, $\mathbf{2}_3$, **3**, **4**) or -15 to 15 MHz (compounds $\mathbf{1}_5$, $\mathbf{2}_1$)).

ruler	dim(J)	dim(t)	2-norm condition number
$\mathbf{1}_3$	50	633	4707
$\mathbf{1}_5$	175	313	490
$\mathbf{2}_1$	50	326	307838
$\mathbf{2}_3$	75	332	54
3	100	526	120499
4	73	351	111651

Table 1: Dimension of time domain t and exchange coupling J in the kernel used for data analysis of different ruler compounds and resulting 2-norm condition number.

1.7. Variation of input distance distribution for the Tikhonov regularization approach

Compound $\mathbf{1}_5$. Figure S17 shows the influence of the input distance distribution on the exchange coupling distribution obtained by Tikhonov regularization for the [Cu-PyMTA]–[Cu-PyMTA] compound $\mathbf{1}_5$. It can be observed that the extracted exchange coupling distributions remain almost unaffected by a mean distance shift of 2 Å, while the quality of the form factor fit decreases. Similarly, an increase or decrease of the width of the distance distribution by 1 Å (Figure S17b) does not alter the exchange coupling distribution, but the form factor oscillations dampen too quickly for the broad distance distribution. A simultaneous change of the width and mean value of the distance distribution evoke deviations in the form factor fits from the experimental data, but not a significant change in the exchange coupling distribution. In summary, smaller variations of the distance distribution do not alter the extracted exchange coupling distributions. These findings enhance the confidence in the assumption of a fixed distance distribution in the exchange coupling fitting approach even if there is an uncertainty in the input distance distribution. The findings also suggest that the distance distribution could be fitted to some extent, as long as relatively tight bounds for the mean distance and standard deviation can be given.

Compound $\mathbf{1}_3$. For [Cu-PyMTA]–[Cu-PyMTA] ruler $\mathbf{1}_3$, we would expect a distance distribution of mean distance r_{mean} = 3.1-3.2 nm and a width of about 1.4 Å based on the corresponding rulers with Mn(II) or Gd(III) as paramagnetic metal ion and a distance shift of about 2 Å as observed for the [Cu-PyMTA]–[Cu-PyMTA] ruler $\mathbf{1}_5$ when compared to the corresponding [Mn-PyMTA]-[Mn-PyMTA] and [Gd-PyMTA]-[Gd-PyMTA] rulers. Figure S18 shows the resulting exchange coupling distributions, for a Gaussian dis-

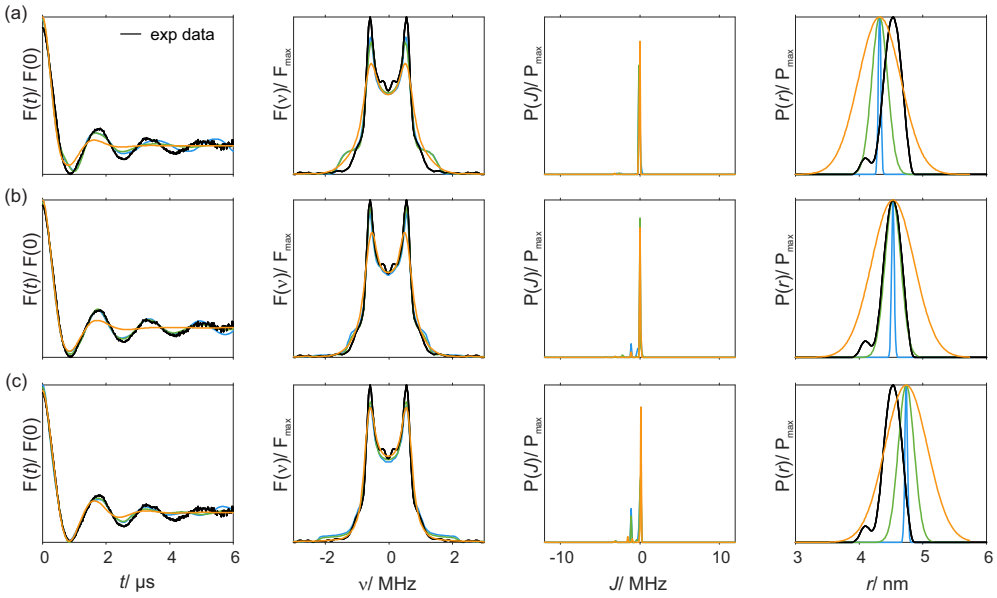

Figure S17: Variation of distance distribution used in the Tikhonov regularization approach to extract the exchange coupling interaction for [Cu-PyMTA]–[Cu-PyMTA] compound $\mathbf{1}_5$. From left to right: Time-domain form factor fits; frequency-domain form factor fits; resulting exchange coupling distribution and input distance distributions. Experimental data are shown in black for comparison. (a) $r_{\text{mean}} = 4.3$ nm, $\sigma_r = 0.03$, 0.13, 0.23 nm; (b) $r_{\text{mean}} = 4.5$ nm, $\sigma_r = 0.03$, 0.13, 0.23 nm; (c) $r_{\text{mean}} = 4.7$ nm , $\sigma_r = 0.03$, 0.13, 0.23 nm.

tance distribution of (a) $r_{\text{mean}} = 2.9$ nm, (b) $r_{\text{mean}} = 3.1$ nm, (c) $r_{\text{mean}} = 3.3$ nm and in all three cases $\sigma_r = 0.04$, 0.14, 0.24 nm. In addition, Figure S18(d) shows the results for a Gaussian distance distribution that fits the longer distance peak resulting from the analysis of the experimental data without consideration of exchange couplings ($r_{\text{mean}} = 2.99$ nm, $\sigma_r = 0.23$ nm) as well as the distance peak resulting from the DEERNet analysis with the *exchange resilient* network ($r_{\text{mean}} = 2.3$ nm, $\sigma_r = 0.5$ nm). In the DEERNet distribution case the contribution of the ferromagnetic coupling around -4 MHz is reduced, but also the fit quality is much lower. In all other cases, the qualitative finding of distributed ferromagnetic couplings from 0 to about -4 MHz, with two main peaks at 0 and -4 MHz is found. For mean distances $r_{\text{mean}} \geq 3.1$ nm a weak contribution of broadly distributed anti-ferromagnetic coupling up to approximately 8 MHz starts to appear.

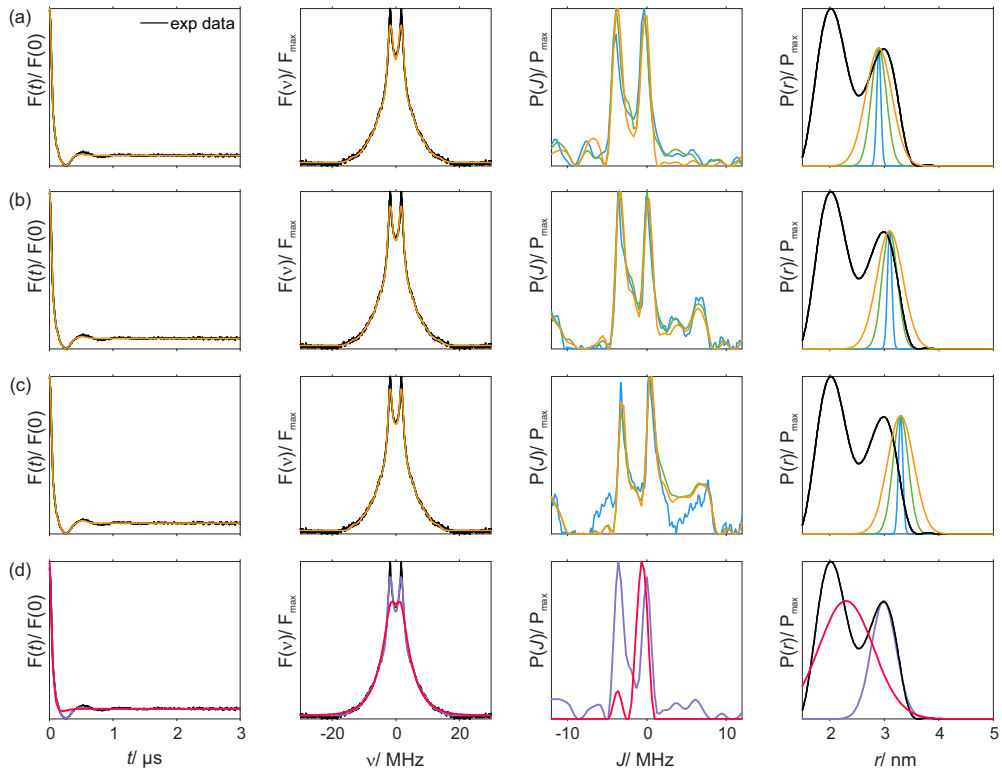

Figure S18: Variation of distance distribution used in the Tikhonov regularization approach to extract the exchange coupling interaction for [Cu-PyMTA]–[Cu-PyMTA] compound $\mathbf{1}_3$. From left to right: Time-domain form factor fits; frequency-domain form factor fits; resulting exchange coupling distribution and input distance distributions. Experimental data are shown in black for comparision. (a) $r_{\mathrm{mean}} = 2.9$ nm, $\sigma_r = 0.04$, 0.14, 0.24 nm; (b) $r_{\mathrm{mean}} = 3.1$ nm, $\sigma_r = 0.04$, 0.14, 0.24 nm; (c) $r_{\mathrm{mean}} = 3.3$ nm , $\sigma_r = 0.04$, 0.14, 0.24 nm; (d) $r_{\mathrm{mean}} = 2.99$ nm, $\sigma_r = 0.23$ nm and $r_{\mathrm{mean}} = 2.3$ nm, $\sigma_r = 0.5$ nm

1.8. Additional neural network analysis

Figure S19 shows the neural network analysis for the remaining compounds. The apparent distance distributions obtained with the *generic* network nicely reproduce Tikhonov regularization data. In particular we want to point out that the neural network-based analysis is able to extract the rather steep RIDME background. However, the *exchange resilient* network is not able to extract the anticipated distance distributions, neither in the presence nor in the absence of exchange interactions.

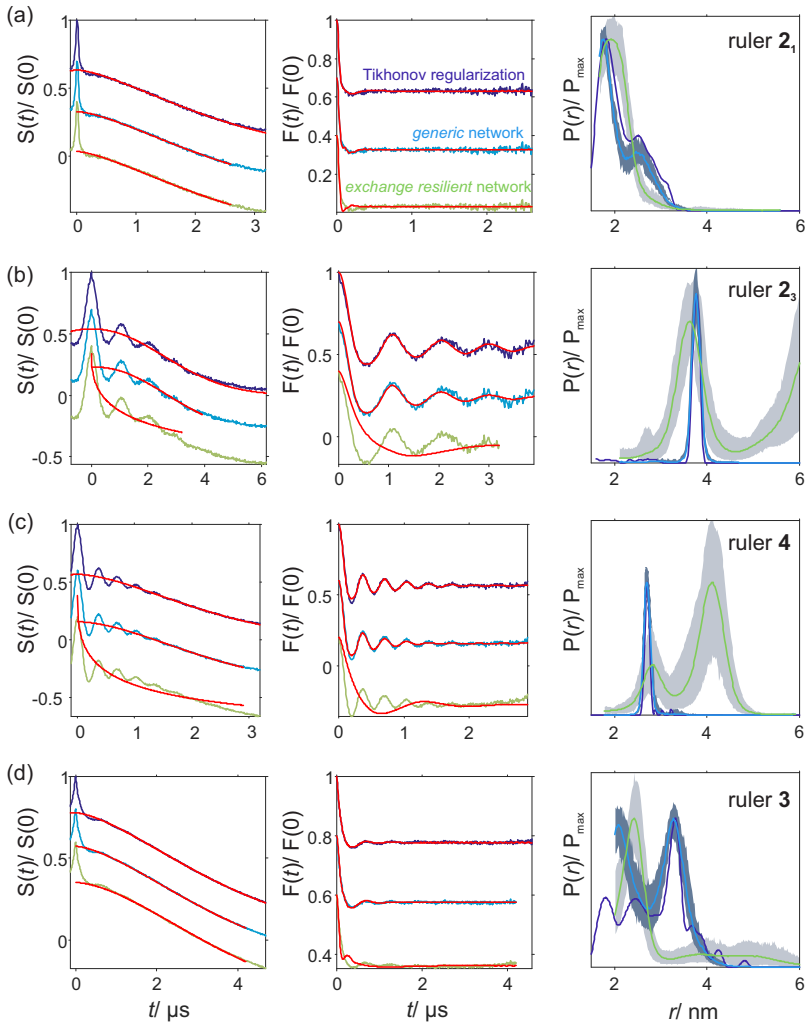

Figure S19: Neural network analysis from RIDME transverse evolution data at 20 K in Q Band. (a) [Cu-PyMTA]-nitroxide ruler $\mathbf{2}_1$, (b) [Cu-PyMTA]-nitroxide ruler $\mathbf{2}_3$, (c) [Cu-TAHA]-nitroxide ruler **4** and (d) [Cu-TAHA]–[Cu-TAHA] ruler **3**. Magenta lines correspond to Tikhonov analysis, blue lines to the *generic* network and green lines to the *exchange resilient* network. From left to right: Primary data and corresponding background fit (red, dashed lines); background-corrected form factors and corresponding fit (red, dashed lines); resulting distance distribution and corresponding uncertainties: dark grey *generic network*, light grey *exchange resilient* network.

1.9. Aggregation Control Experiments

The molecular rulers with the TAHA ligand were not expected to give contributions of exchange coupling at nominal inter-spin distances above ∼

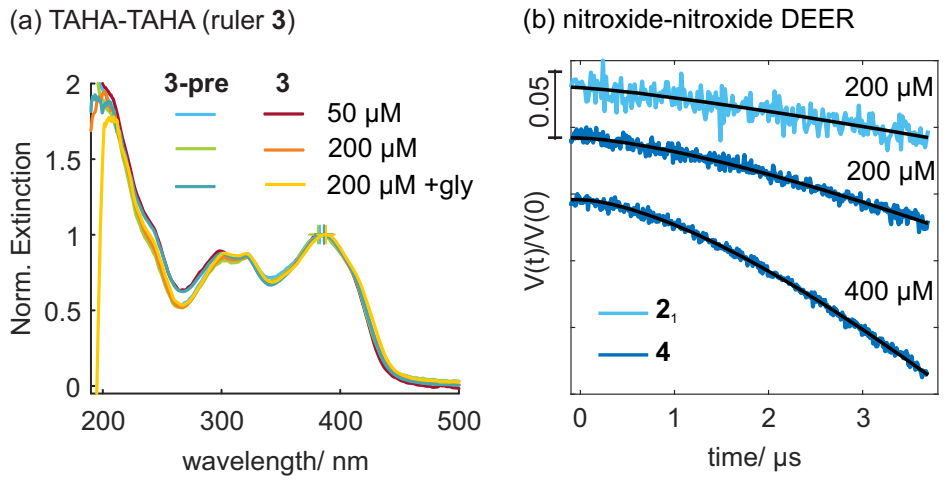

Figure S20: Control experiments to detect potential aggregation of TAHA-based rulers; (a) UV/Vis extinction spectra of [Cu-TAHA]–[Cu-TAHA] ruler **3** and the corresponding unloaded ruler precursor at low (50 μM) and high concentration (200 μM). (b) Q-band primary data of nitroxide-nitroxide DEER at 50 K with the rulers [Cu-PyMTA]-nitroxide $\mathbf{2}_1$ and [Cu-TAHA]-nitroxide **4**. The parameters for the background fit are given in Table 2.

2 nm because for the case of this ligand the conjugated π-system of the effective spacer is separated from the atoms coordinated to the Cu(II) ion by at least three saturated bonds. This led us to investigate (concentration dependent) aggregation as a potential source of additional couplings. The Cu-nitroxide EPR PDS experiments (both RIDME and DEER) were performed at 200 μM ruler concentration in the presence of 50% (deuterated) glycerol, while the UV/Vis data shown in the main text were collected at 50 μM without glycerol. UV/Vis measurements of the [Cu-TAHA]–[Cu-TAHA] ruler **3** at 200 μM without and with glyercol are shown in Figure S20(a). Water, resp. an equivalent water/glycerol mixture was used as blank. The lowest energy peak does not shift upon Cu(II) ion binding even at higher ruler concentration, but there seem to be significant baseline shifts, especially in the UV range below 250 nm. The baseline shift is more pronounced in the presence of 50% (V/V) glycerol (gly), which is equivalent to what was used for the EPR PDS experiments. In principle, one could hypothesize that the baseline shift is induced by the presence of small aggregates in the sample, which affect the light scattering behaviour.

We measured nitroxide-nitroxide DEER on the Cu(II)-nitroxide rulers in order to obtain direct evidence of such aggregation or to exclude this option

(see Figure S20(b)). The data were acquired at 50 K with 16 ns pulse length for both the $\pi/2$ and π pulses of observer and pump spins. The pump frequency was set to the maximum of the nitroxide spectrum, the detection was offset by +100 MHz. The delays were d_1=400 ns d_2=4000 ns. The parameters of the background fit are reported in Table 2. For a perfectly dispersed sample we expect to observe a mono-exponential decay of dimensionality $d = 3$ with a concentration dependent decay rate. Indeed, this holds approximately true for the 200 μM sample of [Cu-PyMTA]-nitroxide ruler $\mathbf{2}_1$, but d is slightly elevated in [Cu-TAHA]-nitroxide ruler **4**. Note that this is exactly opposite to what was found for the contribution of exchange coupling. No significant contribution of exchange coupling was detected for [Cu-TAHA]-nitroxide ruler **4**, whereas there was significant exchange coupling detected in the spectra of [Cu-PyMTA]-nitroxide ruler $\mathbf{2}_1$. This suggests that in the rulers with spectroscopically orthogonal spin labels measured at 200 μM the exchange coupling is dominated by intramolecular mechanisms. To understand why additional couplings were in contrast found for [Cu-TAHA]–[Cu-TAHA] ruler **3**, we point out that the ligand concentration with respect to ruler concentration is doubled compared to [Cu-TAHA]-nitroxide ruler **4**. We thus measured nitroxide-nitroxide DEER of a 400 μM solution of [Cu-TAHA]-nitroxide ruler **4**, which is equivalent to 400 μM [Cu-TAHA], and thus 200 μM [Cu-TAHA]–[Cu-TAHA] ruler **3**. In addition to the expected faster decay from higher absolute spin concentrations we observe that the background can only be well fitted with an even higher dimensionality ($d = 4.6$). No pronounced, resolved oscillations appear, which rather disfavours a head-to-head type of aggregation, where we would expect a rather well defined nitroxide-nitroxide distance of $r \approx 2 \cdot 2.5\text{nm} = 5\text{nm}$. Interestingly, dimensionalities larger than three in DEER can be predicted from theory, and were previously reported in samples that feature an 'excluded volume' around the detected spin.[4] Appearance of this effect at higher concentrations, where the mean intermolecular distance becomes closer to the size of the ruler molecule, is, thus, feasible.

Note that control experiments measured at the maximum of the Cu-TAHA spectrum with 25 μM concentration of [Cu-TAHA]–[Cu-TAHA] ruler **3** did not lead to a reduction of the additional peaks in the distance distribution (see Figure S21) and no significant changes could be observed in the background decay, which is however dominated by spectral diffusion in the RIDME experiment. For the mixing time of 150 μs a small deviation in modulation depth was observed. This may be caused by somewhat different

sample	c /μM	d	rmsd
ruler $\mathbf{2}_1$	200	3.7	0.007
ruler **4**	200	4.3	0.003
ruler **4**	400	4.6	0.002

Table 2: Background fit dimensionality d, and root mean square deviation (rmsd) of background fit for nitroxide-nitroxide DEER at different concentrations c.

T_1 as well as different contributions of the echo crossing artefact.

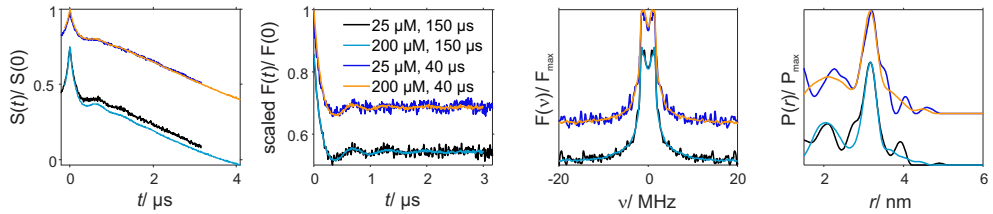

Figure S21: Comparison of Q-band RIDME measurements of [Cu-TAHA]–[Cu-TAHA] ruler **3** at 25 and 200 μM concentration and two different mixing times as color coded. Detected at maximum field and 20 K. From left to right: Primary data; modulation-depth scaled time-domain form factor; normalized frequency-domain form factor; resulting distance distributions.

In combination, these additional results support the assumption that no significant aggregation is induced by the addition of Cu(II) to samples with TAHA ligand, and that it is not enhanced in the presence of glycerol.

1.10. UV/ Vis analysis

The maxima of the UV/Vis spectra of the samples reported in the main text are tabulated in Table 3. The spectra were measured in triplicates and the wavelengths of the positions of the numerical maxima above 350 nm are reported (standard deviations shown in brackets). The average shift between a ruler precursor and the ruler is tabulated as well.

ligand moiety	ruler	main peak/ nm (std. of tripl)	ruler precursor	main peak/ nm (std. of tripl)	shift/ nm
TAHA	**4**	360.7(0.3)	**4**-pre	359.5(0)	-1.2
	3	382.2(0.3)	**3**-pre	384.5(2.3)	2.3
PyMTA	$\mathbf{2}_1$	367.5(0)	$\mathbf{2}_1$-pre	371.8(0.3)	4.3
	$\mathbf{2}_3$	406.3(0.3)	$\mathbf{2}_3$-pre	408.8(1)	2.5
	$\mathbf{1}_1$	364.7(0.8)	$\mathbf{1}_1$-pre	371.5(0)	6.8
	$\mathbf{1}_3$	407.8(0.3)	$\mathbf{1}_3$-pre	412.3(1.4)	4.5
	$\mathbf{1}_5$	422.7(0.6)	$\mathbf{1}_5$-pre	425.8(0.3)	3.1

Table 3: Maxima of the lowest energy bands of the UV/Vis spectra for rulers and corresponding ruler precursors as well as average shift between ruler precursors and rulers.

1.11. CW EPR lineshape analysis

Figure S22 shows the simulated CW EPR lineshapes with corresponding spin Hamiltonian parameters used in the simulations for Cu-PyMTA and Cu-TAHA.

For Cu-PyMTA the analysis of the CW EPR data from our previous work[5] is reproduced here for completeness. Using axial g and A tensors led to deviations between lineshape fit and experimental data around 320 mT, which could only be reduced by assuming rhombic g and A tensors. The relatively large A_y was tested for significance by keeping it fixed at different values (30, 50, 60, 65, 70, 80, 90 MHz) and varying all other parameters as well as varying all fit parameters. The fit quality started to increase from 65 MHz onward and decreased from 90 MHz onward. The resulting fit parameters for fixing A_y between 65 and 90 MHz and varying all other parameters were used to extract the mean and standard deviation as uncertainty for the lineshape parameters of Cu-PyMTA: $g_x = 2.048 \pm 0.001$, $g_y = 2.078 \pm 0.001$, $g_z = 2.253 \pm 0.001$ with strains $g_x\text{strain} = 0.025 \pm 0.001$, $g_y\text{strain} = 0.038 \pm 0.001$, $g_z\text{strain} = 0.035 \pm 0$ and $A_x = 24 \pm 6$ MHz, $A_y = 76 \pm 10$ MHz, $A_z = 510 \pm 5$ MHz with strains $A_x\text{strain} = 4 \pm 4$ MHz, $A_y\text{strain} = 9 \pm 4$ MHz, $A_z\text{strain} = 25 \pm 1$ MHz.[5]

For the Cu-PyMTA complex addition of nitrogen hyperfine couplings, either $A_{iso} = 50$ MHz to determine an upper bound or the largest nitrogen hyperfine couplings from Table 4 ($A_x = A_y = 30$ MHz, $A_z = 48$ MHz), does lead to a reduction of g strain combined with an increase in A strain upon RMSD optimization in EasySpin (Figure S22(c)). However, the couplings remain unresolved within the broad EPR lines and are therefore compatible

with the experimental CW EPR spectrum.

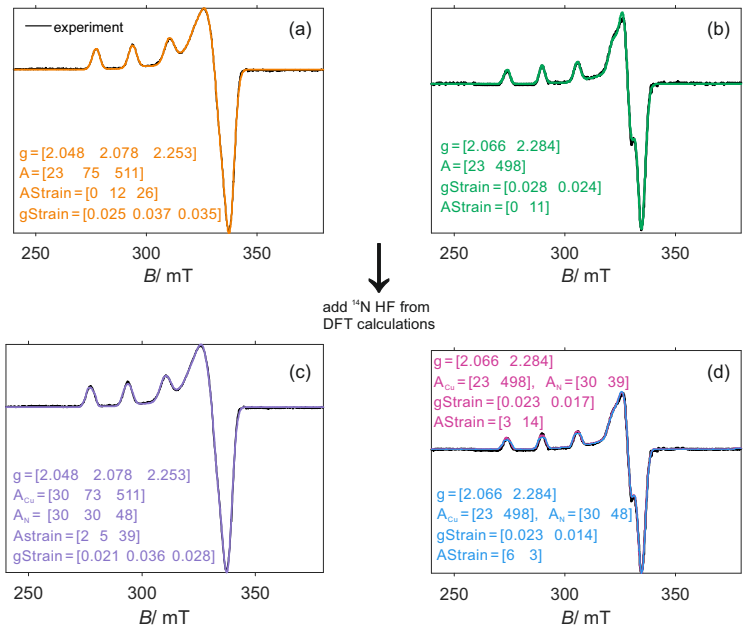

Figure S22: Comparison of experimental (black lines) and simulated low temperature (140 K) CW EPR spectra of Cu(II) complexes in X band. (a, c) Cu-PyMTA, (b, d) Cu-TAHA. (a, b) Neglecting ^{14}N hyperfine couplings and (c, d) including ^{14}N hyperfine couplings.

In comparison, the spectrum of Cu-TAHA can be nicely reproduced using axial tensor geometries (Figure S22(b)). However, in this compound the addition of the largest hyperfine coupling from Table 4 results in some broadening of the CW EPR lineshape of Cu-TAHA as shown in Figure S22(d). An upper limit below which nitrogen hyperfine coupling does not lead to a significant lineshape broadening is estimated as $A_x = A_y = 30$ MHz, $A_z = 39$ MHz, meaning that the nitrogen A_z values needs to be reduced by about 10% compared to the largest value calculated by DFT (largest $A_N = 44$ MHz for Cu-TAHA, Table 5) in order to be consistent with experimental results. In the case of the [Cu-TAHA]–[Cu-TAHA] ruler **3**, also the larger hyperfine couplings computed for Cu-PyMTA remain unresolved ($A_z = 48$ MHz, Figure S23(b)) in the somewhat broader EPR lines. To reproduce the lineshape the g_z/A_z-values needed to be slightly changed compared to Cu-TAHA as presented in Figure S23(a) (red lines). Small further improvement was achieved by also adjusting $g_{x,y}$ (green lines), while varying $A_{x,y}$ yielded no further improvement. These findings indicate that some variation occurs

in the electronic structure of the Cu(II) ion in the [Cu-TAHA]–[Cu-TAHA] ruler **3**. However, the overall fitting quality is lower than for Cu-TAHA.

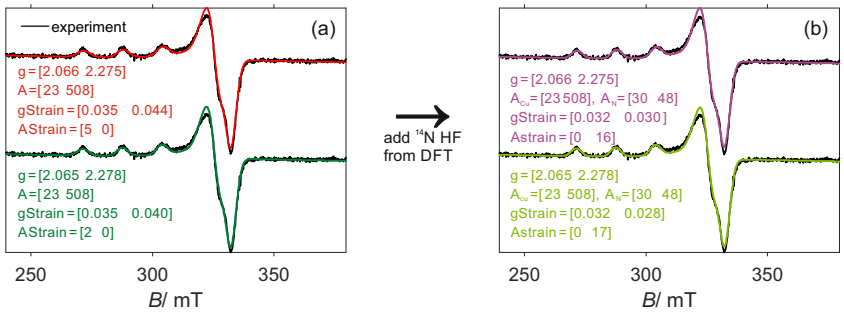

Figure S23: Comparison of experimental (black lines, top and bottom are the same) and simulated low-temperature (140 K) CW EPR spectra for the [Cu-TAHA]–[Cu-TAHA] ruler **3** in X band. (a) Neglecting ^{14}N hyperfine couplings and (b) including ^{14}N hyperfine couplings.

The Peisach-Blumberg plot[6] is presented in Figure S24. It shows that both Cu-PyMTA and Cu-TAHA fall into ambiguous regions of two or three coordinating nitrogens. A tendency towards two copper-coordinating nitrogens is observed for Cu-TAHA, such a coordination is also found in the DFT-optimized geometries described below. For Cu-PyMTA a tendency towards three coordinated nitrogens is observed that is also observed in the DFT-optimized structure with two axial protons (Figure S25(c)).

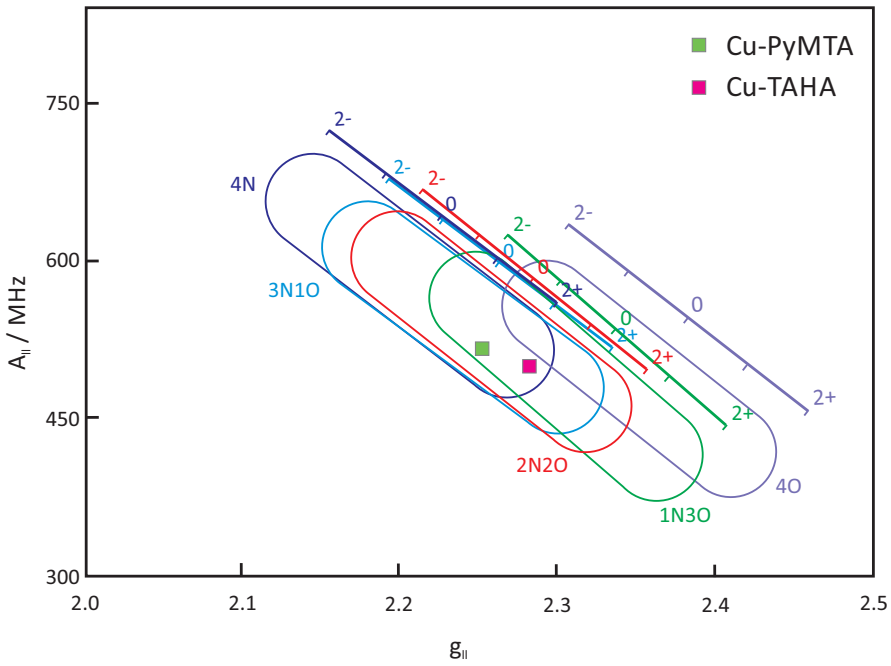

Figure S24: Peisach-Blumberg plot for Cu-PyMTA and Cu-TAHA.

1.12. DFT calculations

Tables 4 and 5 show the calculated DFT parameters for Cu-PyMTA and Cu-TAHA, respectively. For comparison, the first row gives the experimental values extracted from the lineshape fits, where the nitrogen hyperfine couplings $A_{iso} = 50$ MHz for Cu-PyMTA or $A_{iso} = 35$ MHz for Cu-TAHA were taken as an estimate for an upper bound of this coupling and validated that they do not lead to resolved splittings or significant broadening in the lineshape fits.

For Cu-PyMTA, comparing the g and A tensors from the DFT calculations to the experimental ones (Table 4), we observe the following trends. We find only small variations of the g and A tensors upon interchange of the two hybrid functionals B3LYP and PBE0. In contrast, changing the basis set used for Cu(II) from the standard triple zeta basis to CP(PPP), which is optimized for core properties, we find a significant improvement of the Cu A tensor values, while the g tensor remains similar. Yet the calculated g and Cu(II)-A tensors fail to reach quantitative agreement. Qualitatively, we find that the near-axial symmetry of the g tensor is only reproduced in the case of two axial protons. The ^{14}N hyperfine couplings are virtually unaf-

fected by the choice of functional and basis set and differ only among the different protonation states. Yet, since this coupling is not resolved in the EPR spectra, we can only ascertain an upper bound of $A(^{14}\mathrm{N}) = [30, 30, 48]$ MHz that is in agreement with the experimentally-derived upper bound of $\sim$50 MHz. This ^{14}N hyperfine coupling corresponds to ca. 13% spin density on the nitrogens, of which there are three directly coordinating Cu(II) here in the DFT-optimized geometries (Figure S25), in agreement with the Peisach-Blumberg analysis (Figure S24).

Figure S25 shows the optimized geometries and spin density distributions for the different protonation states of Cu-PyMTA. The geometry optimized in the presence of two axial protons results in calculated g tensors with near axial symmetry that qualitatively match the experiment and shows a spin density of 64% on Cu(II) along with an equally distributed spin density of about 10% on each of the three nitrogens. The coordination by three nitrogens is in agreement with the Peisach-Blumberg plot (Figure S24). In the other two cases, no protons or two in-plane protons, the g tensor symmetry does not match the experimental values. The nitrogens are further apart from the Cu(II)-ion in these geometries and carry less spin density.

Therefore, for Cu-PyMTA, out of these structures the model with two axial protons is found to have the best resemblance to the experimental parameters, and hence we conclude, corroborated by the experimental hyperfine couplings and g tensor symmetry, that the spin density is mostly localized on the Cu(II) ion and its three directly coordinating nitrogens, with only insignificant delocalization over the other atoms of the pyridine ring. Note further that in the DFT calculations we only accounted for the solvent implicitly. Including the explicit water would certainly result in formation of some hydrogen bonds to carboxylic groups, which might substitute the two axial protons in our best DFT model, and thus remove the apparent inconsistency with respect to the expected full deprotonation[7] of the Cu-PyMTA under our experimental conditions (pH 7.0).

For Cu-TAHA Table 5 gives the calculated DFT parameters in comparison with the experimental values extracted from the CW EPR lineshape fit. The experimental ^{14}N hyperfine coupling only represents an upper bound that is still in agreement with the experimental CW EPR spectrum. For all of the four protonation states considered for Cu-TAHA using the def2-TZVPP basis for the Cu(II) ion results in qualitatively wrong copper hyperfine couplings, while the couplings qualitatively agree when the CP(PPP) basis is used for the Cu(II) ion, at least for the first three protonation states,

	g_1	g_2	g_3	$A_{1,\mathrm{Cu}}$	$A_{2,\mathrm{Cu}}$	$A_{3,\mathrm{Cu}}$	$A_{1,\mathrm{N}}$	$A_{2,\mathrm{N}}$	$A_{3,\mathrm{N}}$
Exp. fit	2.048	2.078	2.253	30	73	511	50[e]	50[e]	50[e]
No prot[a]	2.005 (0)	2.204 (0)	2.238 (0.001)	140 (15)	246 (15)	811 (13)	9 (0)	9 (0)	13 (0)
No prot[b]	2.005	2.202	2.235	128 (5)	228 (6)	393 (7)	9 (0)	9 (0)	13 (0)
No prot[c]	2.005	2.183	2.212	161	269	822	10	10	13
No prot[d]	2.005	2.178	2.210	112	215	399	10	10	13
2 axial prot[a]	2.033 (0)	2.097 (0)	2.189 (0.001)	179 (20)	236 (18)	531 (19)	28 (1)	28 (1)	45 (0)
2 axial prot[b]	2.032 (0)	2.095 (0.001)	2.182 (0)	115 (4)	159 (1)	506 (2)	28 (1)	28 (1)	46 (0)
2 axial prot[c]	2.029	2.086	2.166	145	257	544	30	30	48
2 axial prot[d]	2.028	2.084	2.161	98	170	477	30	30	48
2 in-plane prot[a]	2.007 (0)	2.173 (0)	2.207 (0)	124 (16)	320 (17)	820 (14)	14 (1)	14 (1)	22 (1)
2 in-plane prot[b]	2.003 (0)	2.169 (0)	2.202 (0)	43 (4)	230 (5)	415 (6)	14 (1)	14 (1)	23 (0)
2 in-plane prot[c]	2.007	2.152	2.185	148	353	828	16	16	25
2 in-plane prot[d]	2.007	2.159	2.181	16	214	417	16	16	26

Table 4: Calculated EPR parameters in comparison to experimental parameters obtained from lineshape fitting for Cu-PyMTA. [a] PBE0, def2-TZVPP basis on all atoms, [b] PBE0, def2-TZVPP basis except for Cu(II) (CP(PPP)). Numbers in parentheses give the deviation for calculations with *vs.* without the RIJCOSX approximation. [c] B3LYP, def2-TZVPP basis on all atoms, [d] B3LYP, def2-TZVPP basis except fo Cu(II) (CP(PPP)). [e] represents an upper bound that is still compatible with the experimental CW EPR spectrum.

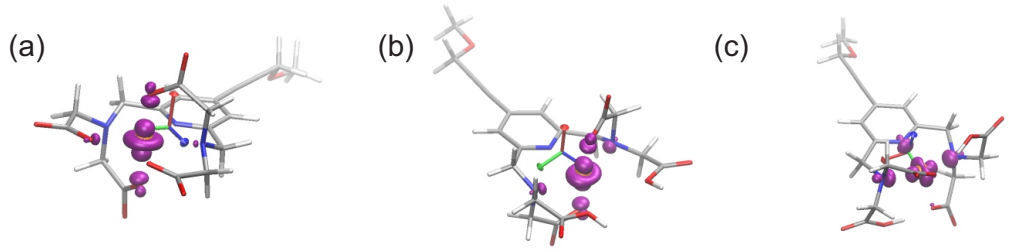

Figure S25: Optimized geometries, spin density distributions (contour level 1%) and g tensor orientation for Cu-PyMTA. (a) No protons, (b) two in-plane protons and (c) two axial protons. Calculated with the functional PBE0 (with RIJCOSX approximation) and def2-TZVPP basis except for Cu(II) (CP(PPP)).

namely no protons, 2 protons and 4 protons (opposite protons removed). For these three states also the g tensor symmetry reflects the experimentally observed tensor symmetry. The fourth state, with four neighboring protons removed, showed the largest deviations for the copper hyperfine couplings as well as a clearly overestimated g tensor anisotropy. In contrast, the nitrogen hyperfine couplings are neither strongly affected by the different protonation states, nor by the basis sets for the Cu(II) ions and show maximum values of $A_{\mathrm{N,DFT}} = (30, 30, 44)$ MHz, which is somewhat larger than the experimental upper bound of an $A_{\mathrm{iso}} = 35$ MHz or an axial nitrogen hyperfine tensor of [30 39] MHz. Figure S26 shows the optimized geometries and spin density distributions for the different protonation states of Cu-TAHA. In case of two opposite protons removed, the third ligand arm drifts most strongly away - likely due to the neutral caboxylic groups on the ligand arm. A deviation towards a more rhombic system is observed when two neighbouring protons are removed (Figure S26d). In all protonation states, two out of the three nitrogens are located at a closer distance to the Cu(II) ion (e.g. ca. 2.1 vs. 2.8 Å for Figure S26 a & b), which is in agreement with the Peisach-Blumberg plot presented above, and only these two nitrogens carry significant spin density ($\sim 10\%$) along with the neighbouring oxygen atoms (up to 10%), while most of the spin density (60-70%) is located on the Cu(II) ion. The optimized geometries indicate that not necessarily all ligand arms of TAHA take part in complexation of the Cu(II)-ion and that different complexation geometries may exist. The nitrogen hyperfine couplings are somewhat smaller than in

PyMTA, which is in agreement with the lineshape simulations. Note that in the literature also dinuclear Cu(II) complexes have been observed with a similar ligand.[8] This can be excluded in our case based on the CW EPR spectra. Therefore, while we cannot distinguish the different protonation states for Cu-TAHA, we do conclude from the spin densities validated by the experimental hyperfine couplings and g tensor symmetry that the majority of the spin density is located on the Cu(II) ion and on two directly coordinating nitrogens.

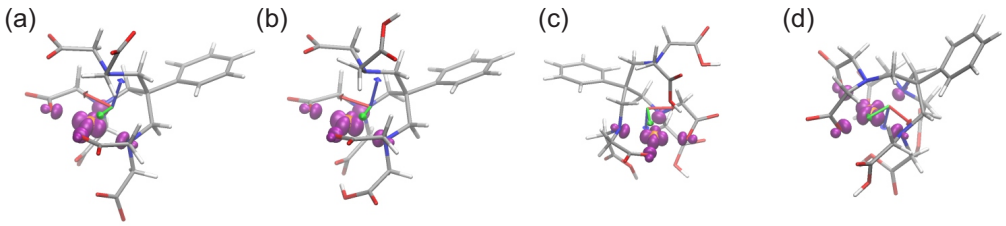

Figure S26: Optimized geometries, spin density distributions (contour level 1%) and g tensor orientation for Cu-TAHA. (a) No protons, (b) two protons, (c) four protons - two opposite protons of the fully protonated starting structure removed and (d) four protons - two neigbouring protons of the fully protonated starting structure removed. Calculated with PBE0 functional, RIJCOSX approximation and def2-TZVPP basis except for Cu(II) (CP(PPP)).

	g_1	g_2	g_3	$A_{1,\mathrm{Cu}}$	$A_{2,\mathrm{Cu}}$	$A_{3,\mathrm{Cu}}$	$A_{1,\mathrm{N}}$	$A_{2,\mathrm{N}}$	$A_{3,\mathrm{N}}$
Exp. fit	2.066	2.066	2.284	23	23	498	30[e]	30[e]	39[e]
No prot[a]	2.059 (0)	2.068 (0)	2.202 (0)	260 (20)	370 (20)	401 (21)	27 (1)	27 (1)	41 (0)
No prot[b]	2.054	2.063	2.194	1 (1)	27 (1)	592 (12)	27 (1)	28 (0)	42 (0)
No prot[c]	2.059	2.066	2.202	221	395	426	29	29	43
No prot[d]	2.049	2.056	2.172	18	47	562	29	30	44
2 prot[a]	2.055 (0.001)	2.062 (0)	2.195 (0)	271 (19)	358 (19)	379 (20)	28 (0)	28 (0)	41(0)
2 prot[b]	2.051 (0.001)	2.059 (0.002)	2.185 (0.003)	3 (4)	6 (5)	603 (0)	28 (1)	28 (1)	42 (0)
2 prot[c]	2.048	2.055	2.173	233	383	404	29	30	44
2 prot[d]	2.046	2.052	2.164	8	29	571	30	30	44
4 prot op[a]	2.049 (0)	2.054 (0)	2.176 (0)	306 (15)	311 (13)	315 (12)	27 (1)	28 (0)	41 (0)
4 prot op[b]	2.048 (0.001)	2.053 (0)	2.172 (0.001)	45 (3)	54 (3)	633 (2)	25 (0)	25 (0)	40 (0)
4 prot op[c]	2.044	2.048	2.156	269	330	340	29	29	43
4 prot op[d]	2.042	2.047	2.159	25	34	598	30	30	44
4 prot ne[a]	2.038 (0.001)	2.110 (0.002)	2.227(0)	138 (19)	314 (18)	549 (16)	22 (1)	22 (1)	34 (0)
4 prot ne[b]	2.038	2.107	2.226	42 (2)	176 (4)	466 (2)	22 (1)	22 (1)	35 (0)
4 prot ne[c]	2.034	2.097	2.199	109	332	557	23	24	26
4 prot ne[d]	2.034	2.095	2.195	26	180	442	24	24	36

Table 5: Calculated EPR parameters in comparison to parameters obtained from lineshape fitting for Cu-TAHA.[a] PBE0, def2-TZVPP basis on all atoms, [b] PBE0, def2-TZVPP basis except for Cu (CP(PPP)). The parentheses () gives the deviation when using the RIJCOSX approximation. [c] B3LYP, def2-TZVPP basis on all atoms, [d] B3LYP, def2-TZVPP basis except for Cu (CP(PPP)). [e] represents an upper bound that is still compatible with the experimental CW EPR spectrum. There were two different starting structures with 4 protons: op = opposite protons were removed, ne = neighbouring protons were removed.

References

[1] K. Keller, V. Mertens, M. Qi, A. Nalepa, A. Godt, A. Savitsky, G. Jeschke, M. Yulikov, Computing Distance Distributions from Dipolar Evolution Data with Overtones: RIDME Spectroscopy with Gd(III)-Based Spin Labels, Phys. Chem. Chem. Phys. (2017).

[2] I. Ritsch, H. Hintz, G. Jeschke, A. Godt, M. Yulikov, Improving the accuracy of Cu(II)-nitroxide RIDME in the presence of orientation correlation in water-soluble Cu(II)-nitroxide rulers, Phys. Chem. Chem. Phys. 21 (2019) 9810–9830.

[3] G. Jeschke, V. Chechik, P. Ionita, A. Godt, H. Zimmermann, J. Banham, C. R. Timmel, D. Hilger, H. Jung, DeerAnalysis2006—a comprehensive software package for analyzing pulsed ELDOR data, Appl. Magn. Reson. 30 (2006) 473–498, http://www.epr.ethz.ch/software.html.

[4] D. R. Kattnig, J. Reichenwallner, D. Hinderberger, Modeling excluded volume effects for the faithful description of the background signal in double electron–electron resonance, J. Phys. Chem. B 117 (2013) 16542–16557.

[5] F. D. Breitgoff, K. Keller, M. Qi, D. Klose, M. Yulikov, A. Godt, G. Jeschke, UWB DEER and RIDME distance measurements in Cu(II)–Cu(II) spin pairs, J. Magn. Reson. (2019) 106560.

[6] J. Peisach, W. Blumberg, Structural implications derived from the analysis of electron paramagnetic resonance spectra of natural and artificial copper proteins, Archives of Biochemistry and Biophysics 165 (1974) 691–708.

[7] W. W. Xie, P. R. Tremaine, Thermodynamics of Aqueous Diethylenetriaminepentaacetic Acid (DTPA) Systems: Apparent and Partial Molar Heat Capacities and Volumes of Aqueous H_2DTPA^{3-}, $DTPA^{5-}$, $CuDTPA^{3-}$, and Cu_2DTPA^{-} from 10 to 55°C, J. Solution Chem. 28 (1999) 291–325.

[8] S. Feng, L. Ma, G. Feng, Y. Jiao, M. Zhu, Dinuclear copper (II) complexes hold by crab-shaped pincer ligands: Syntheses, structures, luminescent and magnetic properties, J. Mol. Struct. 1059 (2014) 27–32.